

RESEARCH ARTICLE | AUGUST 24 2022

# NanoLBIC characterisation of silicon solar cells using a laser pick-up unit

Yifu Shi; Mingzhe Yu; Mohsen Goodarzi; Martin Voss; En-Te Hwu; Ruy Sebastian Bonilla 



AIP Conf. Proc. 2487, 030009 (2022)

<https://doi.org/10.1063/5.0089328>



CrossMark

## Articles You May Be Interested In

Solar Cells Noise Diagnostic and LBIC Comparison

*AIP Conference Proceedings* (July 2007)

The role of localized junction leakage in the temperature-dependent laser-beam-induced current spectra for HgCdTe infrared focal plane array photodiodes

*J. Appl. Phys.* (November 2013)

Screening of high-power diode laser bars by optical scanning

*Appl. Phys. Lett.* (November 2005)

500 kHz or 8.5 GHz?  
And all the ranges in between.

Lock-in Amplifiers for your periodic signal measurements



Find out more



# NanoLBIC Characterisation of Silicon Solar Cells Using a Laser Pick-up Unit

Yifu Shi<sup>1</sup>, Mingzhe Yu<sup>1</sup>, Mohsen Goodarzi<sup>1</sup>, Martin Voss<sup>2</sup>, En-Te Hwu<sup>2</sup>, & Ruy Sebastian Bonilla<sup>1, a)</sup>

<sup>1</sup>*Department of Materials, University of Oxford, Parks Road, Oxford, OX1 3PH, United Kingdom.*

<sup>2</sup>*The Danish National Research Foundation and Villum Foundation's Centre for Intelligent Drug Delivery and Sensing Using Microcontainers and Nanomechanics (IDUN), Department of Health Technology, Technical University of Denmark, 2800 Kgs. Lyngby, Denmark.*

<sup>a)</sup> Corresponding author: sebastian.bonilla@materials.ox.ac.uk

**Abstract.** An innovative blue laser nano-LBIC system is designed and built, demonstrating capabilities as a versatile system for the optoelectronic characterisation of solar cells. A laser pick-up unit is used here to achieve a highly focused laser beam with a full width half maximum as low as 250 nm on the surface of a PERC solar cell. The quality of the resulting LBIC map is evaluated by cross-comparisons with optical micrographs on the same region of the PERC cell. LBIC imaging of laser doped emitters using 405 nm and 650 nm lasers reveals shallow locations of introduced structural defects, which are observed from the higher photocurrent loss in the image obtained by 405 nm photogeneration. A high-resolution map is generated to show current variation related to the surface texture of the cells, at a scale below one micron. Despite no image optimisation or filtering, the results indicate that the lateral resolution of our nano-LBIC system is comparable to that of complex confocal laser microscope-based systems. Our system can enable fast and point-of-manufacture visualisation of recombination inside photovoltaic devices with sub-micron spatial resolution without the need for complex optical or vacuum based systems.

## INTRODUCTION

Light beam induced current (LBIC) characterisation provides a 2D map of the short circuit photo current  $I_{sc}$  generated by a scanning light beam. LBIC measurements offer an effective method to spatially resolve the photo-response variations of a device, for example to characterise losses at defects in photovoltaic cells. Theoretical work has been done in history to interpret LBIC scans of defects in silicon, enabling defect recombination properties to be linked to the current profile [1]–[4]. Recent applications of LBIC see its efficacy in characterizing LID [5] and PID [6] in PERC cells and analysing defect behaviours under passivation processes [7][8]. A  $\mu$ LBIC system utilises a highly focused laser beam to produce photocurrent map at micrometre resolutions. The excitation volume by such a narrow laser beam can be sufficiently small to be compared with the resolution result of the electron beam induced current (EBIC) technique [9]. LBIC systems, unlike the scanning electron microscope based EBIC, do not require any vacuum environment and has no charging effects on specimens, hence providing more versatility in measurements.

The minimum spot size that a LBIC system can achieve is determined by the focusing optics as well as the diffraction limit of the laser wavelength used. Reported  $\mu$ LBIC systems can be an adaption of a confocal laser scanning microscope [6][10] or feature a home-made focusing system with microscope objectives and focusing lenses with micrometric movement [11]. Additionally, the local photocurrent mapping resolution around a defect structure is not only related to the laser spot size, but also dependent on the lifetime of excited carriers in the material investigated. It has been previously demonstrated that sub-micron LBIC characterisation can be achieved in confocal systems, at the expense of a costly and sophisticated optical setup [11][12]. An inexpensive and adaptable LBIC system for facile and versatile sub-micron characterisations will be highly beneficial for research and development in both academic and industrial environments.

## SETUP DESCRIPTION

A nano-LBIC system based on a laser pick-up unit (LPU) is designed and implemented in this study. The laser pick-up is a compact unit integrated with optics and electronics typically used for reading/writing data from/to an optical disk. The standard size of the data pit and the track pitch on a Blu-ray disc are 130 nm and 320 nm [13], respectively. Accordingly, the full width at half maximum of the focused polarised laser beam is estimated to be around 250 nm for the 405 nm blue laser on an optical disk [13][14]. Figure 1 (a) shows the internal components of the LPU used in this work which is a simple and typical laser pick-up unit with two separate optical paths. One path is for the 405 nm laser used for Blu-ray data transfer and the other is shared between 650 and 780 nm lasers for DVD and CD data transfers, respectively. Figure 1 (b) illustrates the elements of the optical path for the blue laser beam, from the laser diode to the specimen, and back to the photodiode. These components enable the system to obtain sub-micron level excitation in solar cell devices, leading to the high-resolution images of photocurrent mapping. The laser power used in this study is ranged from 20  $\mu$ W to 50  $\mu$ W as measured by an external laser power meter.

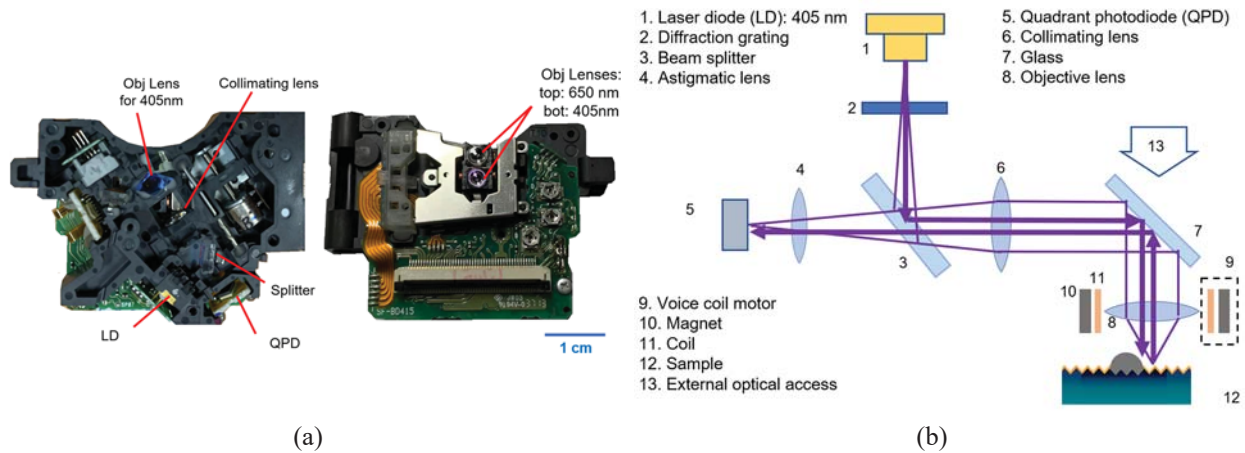


**FIGURE 1.** The laser pick-up unit used as the illumination source for the nano-LBIC system. (a) Photograph of the LPU from top view (left) and bottom view (right) with a 1 cm scale. (b) Optical path for the 405 nm blue laser with a list of laser modules, sensors and actuators.

The key function of the LPU is to ensure the beam is at its minimum width when it is focused on the sample's surface. This is performed by measuring a focus error signal (FES) of the laser relative to the sample surface. The LPU utilises an astigmatic optical path with a quadrant photodiode (QPD) detector to generate the FES using the reflected beam profile on the QPD [15]. Examples of detected FES from the surfaces of a bronze sheet and a finished solar cell are shown in Fig. 2 as a function of the objective lens vertical position. The objective lens (8 in Fig. 1 (b)) is moved vertically by varying the voltage applied to a voice coil motor actuator (9 in Fig. 1 (b)). As marked on Fig. 2 (a), the astigmatic reflected beam will have a changing elliptical profile at a limited range from the best focus point, resulting in a S-shaped FES curve. The focal point of the laser beam can be found when the reflected beam spot on the photodiode quadrants is symmetrical, which corresponds to the midpoint of the S-shaped FES curve. Comparison between the signals from two surfaces also reveals the impact of the surface texture on signal-to-noise ratio of the FES signal acquired. Since silicon solar cells are textured and deposited with an anti-reflection coating, the stability the S-shape profiles obtained from the cell surface is substantially worse than for a flat metal surface.

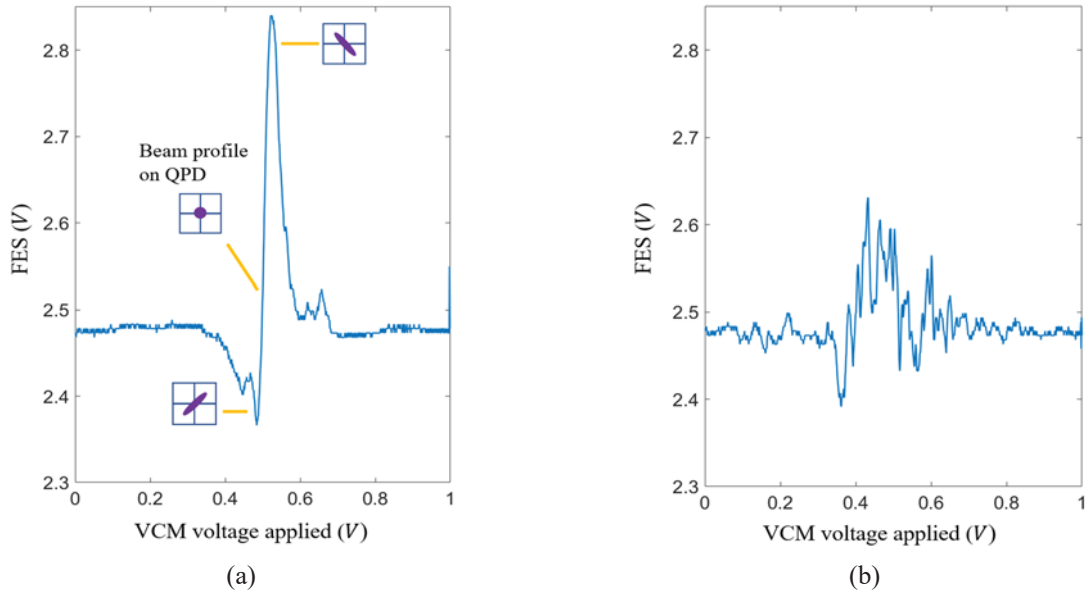


**FIGURE 2.** Example of focus error signal curves detected by the QPD vs voice coil motor voltage at the same gain. (a): from a reflective bronze sheet surface, (b): from a finished solar cell front surface.

Figure 3 shows the schematic diagram of the mechanical setup and signal flows of the nano-LBIC system based on motorised XY stages. Variables such as laser power and the objective lens position are controlled by analogue signals via a customised board through a NI I/O DAQ device in a LabVIEW environment. Prior to each measurement, the objective lens is actuated vertically to the in-focus position according to the FES curve obtained. The VCM can adjust the working distance within an approximately 1000  $\mu\text{m}$  range. The laser generated photocurrent in the cell in the order of  $\mu\text{A}$  is measured by a Keithley 236 Source Measure Unit (SMU). The entire setup is put on a rubber pad for vibration isolation and covered with a light tight enclosure. A 2D current map is then constructed in conjunction with the mechanical raster scanning movement of the sample stage. This scanning is performed by two motorised and feedbacked translation stages at step size as low as 50 nm. The largest area that can be mapped with this set up is  $2.5 \times 2.5 \text{ cm}^2$ . It should be noted that a stable and well-focused narrow excitation is not the only condition to obtain photocurrent maps at high spatial resolution. The mechanical scanning movement performed by the motorised stages also needs to be free of fluctuations or drifts, and the focal point must be maintained throughout a scan.

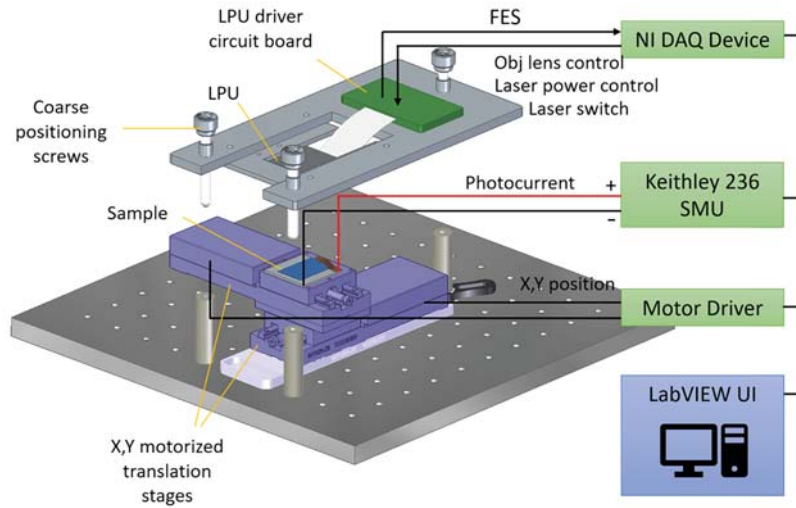


**FIGURE 3.** System setup with motorised X-Y stages, including electronic signal flows

## RESULTS AND DISCUSSION

Two similar types of standard industrial p-type mono PERC cells (PERC A & PERC B) with the same laser doped selective emitters were investigated. A schematic of the front side of the finished PERC cells is shown in Fig. 4. The selective  $n^{++}$  emitter region width ( $\sim 130 \mu\text{m}$ ) is larger than the metal contacts width ( $\sim 30 \mu\text{m}$ ) for the correct alignment of screen-printed Ag paste with the laser doped region. A surface layer of enhanced recombination has been reported after laser doping due to the higher phosphorous concentrations and extra lasering-introduced defects [16][17]. Figure 5 shows SEM and EBIC images of the front side metallisation of a PERC A cell. The reduction in collection efficiency in the  $n^{++}$  region can be observed from the darker fringe adjacent to the Ag fingers in the EBIC image. The carrier injection depth/volume of the electron beam is dependent on the beam energy (details of which can be found in previous EBIC studies [16][18]), analogous to the fact that light wavelength determines the injection depths of carriers. We include these images here to use as a benchmark for the resolution quality of our nano-LBIC system.

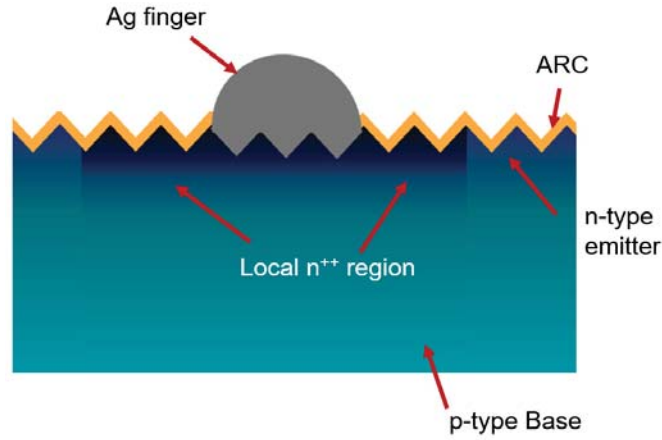


**FIGURE 4.** Structure of the front side of industrial PERC cell samples (not to scale).

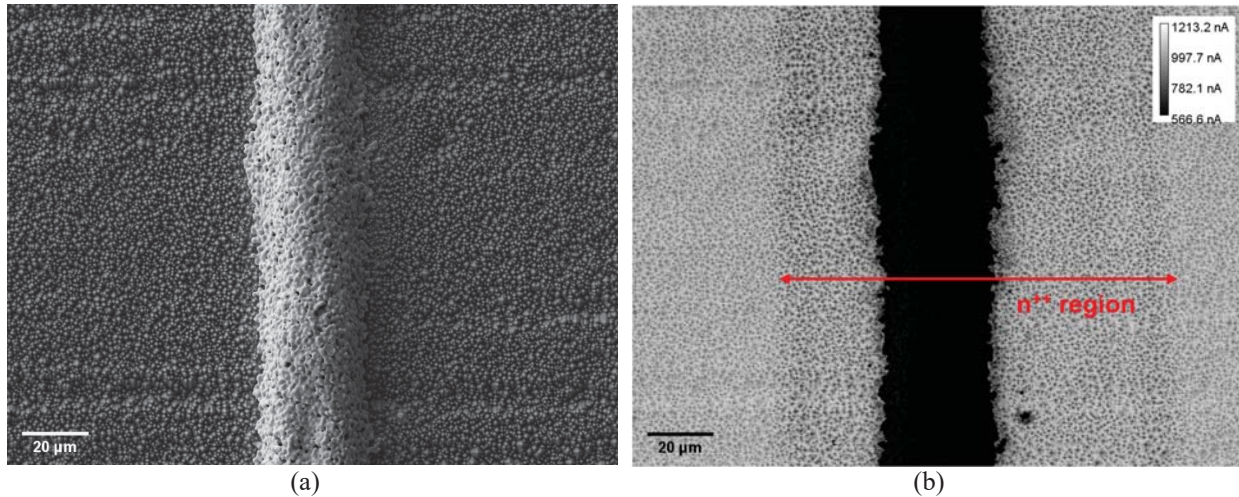


**FIGURE 5.** (a) SEM image of front side metallisation of sample PERC A. (b) EBIC image of the same region with beam energy of 10 kV. Current level is plotted in grey scale as given in the calibration colour bar.

## Stability and Reliability of the Nano-LBIC Setup

A low magnification LBIC map of the PERC A front metallisation with the scanning step size of  $2\text{ }\mu\text{m}$  was obtained. After scanning, the same location was imaged under an optical microscope for comparison. The correlated LBIC and optical images are shown in Fig. 6. The sample surface was marked by a diamond scribe pen for indication to allow easy alignment of the map with the optical micrograph. The precise alignment of the scribe mark between two images in Fig. 6 confirms the sufficient mechanical stability during the LBIC scanning at micrometre scale. The scribing of the surface is causing structural damage into the surface passivation layers and the front side uniform emitter layer, which results in regions of low photocurrent collection (marked with grey arrows). It is also evident that the laser-doped  $n^{++}$  selective emitter is leading to a region of reduced photocurrent which is consistent with the EBIC measurements. Notably these LBIC and optical micrographs have not had any data processing done, showing the excellent imaging quality achieved before any sophisticated noise reduction methods are implemented.

The current does not fall to a zero at the metal fingers despite the fact scans are conducted in darkness with negligible ( $<0.1\text{ nA}$ ) current background while the laser is off. The non-zero current at the fingers can be attributed to a proportion of scattered light from fingers and which is reflected again from the LPU bottom surface and reach back the cell. The distance from the sample surface to the LPU bottom can be as small as  $\sim 1\text{ mm}$  determined by the short working distance of the objective lens.

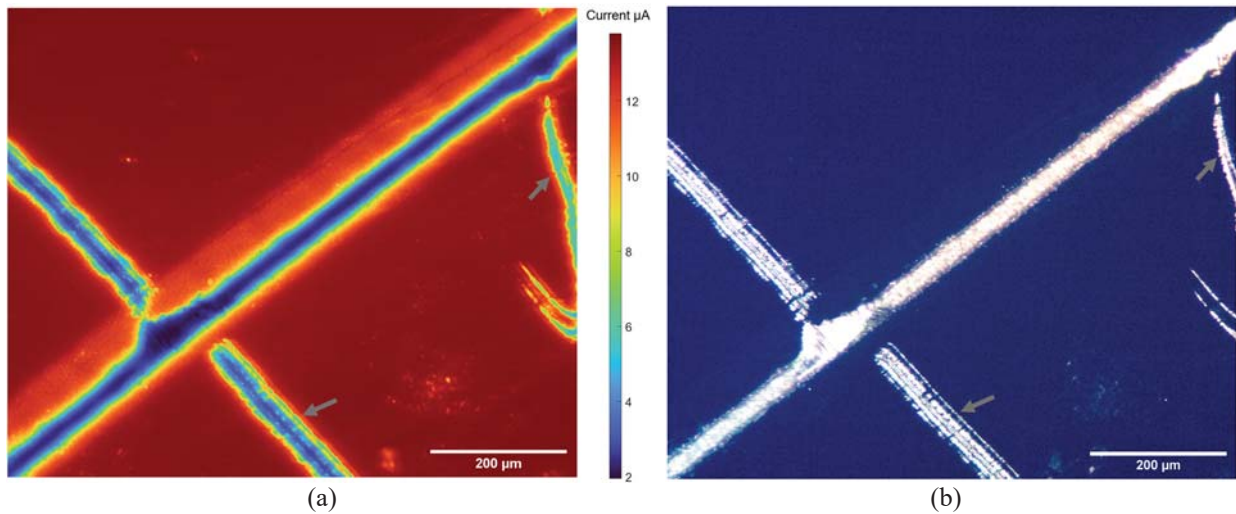


**FIGURE 6.** (a) 405 nm LBIC map of PERC cell A front metallisation with marks, pixel resolution  $2\text{ }\mu\text{m}$ , pixel dwell time  $0.48\text{ s}$ . The colour scheme used for plotting the current map is given as the colour bar. (b) Optical micrograph of the same region.

## The Effect of Photoinjection Wavelength

The LPU used integrates a  $650\text{ nm}$  red laser source along with the  $405\text{ nm}$  blue laser source. Here a  $1\text{ }\mu\text{m}$  scanning step size is used to generate LBIC maps of the front metallisation of a PERC B sample with both wavelengths. The images are of the same sample at different locations. The resulted LBIC images and the measured currents along the lines across the region of interest are shown in Fig 7. The Ag contacts are noticeable in both images with the width of around  $30\text{ }\mu\text{m}$  with the corresponding current profile decreased at the contact. The advantage of comparing between the LBIC maps for two injection wavelengths is the ability to estimate the depth of the damage caused by the laser doping process for selective emitters. An evident difference when mapping with different light sources is the LBIC current contrast in the lasered  $n^{++}$  region compared to the undamaged region. As calculated from the line profile on the blue laser map, the photocurrent at the lasered region (averaged over  $30\text{ }\mu\text{m}$ ) is  $0.91$  times that of the undamaged region. For the red laser map that number is  $>0.97$ . This illustrates that laser doping is leading to a higher loss of collection efficiency under blue wavelength compared to the red wavelength. Considering the absorption depths of  $405\text{ nm}$  and  $650\text{ nm}$  light in Si:  $0.13\text{ }\mu\text{m}$  and  $3.56\text{ }\mu\text{m}$  respectively [19], this indicates that a significantly higher density

of active recombination centres must be presented in a thin surface layer in the  $n^{++}$  selective emitter region. This confirms with previous observations that the laser doping process introduces structural defects in the first hundreds of nanometres from the surface, but such defects are not influential to photogeneration deeper than 1 micrometre. In conclusion, by using the two wavelengths we have revealed the damage inside a thin surface layer from laser doping.

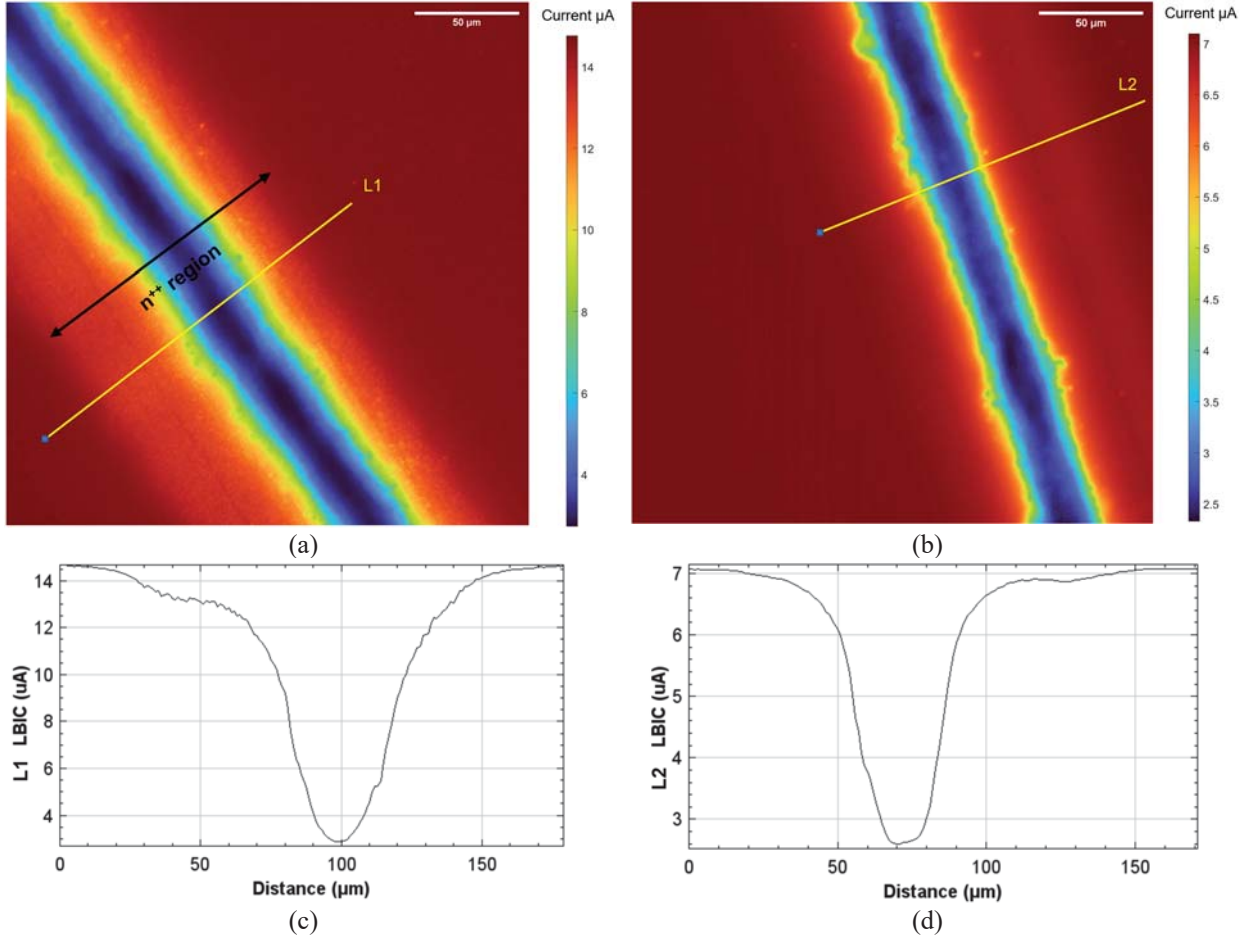


**FIGURE 7.** (a) 405 nm & (b) 650 nm LBIC maps of PERC cell B front metallisation. pixel resolution 1  $\mu\text{m}$ , pixel dwell time 0.45s. The maps are of different metal fingers from the same cell sample. Lines L1 and L2 used for line profiles are marked on the maps respectively. (c) & (d) LBIC current line profiles of across the lasered region and Ag finger.

### Characterisation with Sub-micron Resolution

The designed and built LBIC setup has the capability of the optical characterisation at a submicron resolution when the 405 nm laser is used. Figure 8 (a) presents an SEM micrograph illustrating the well-known pyramidal texture on the surface of a monocrystalline solar cell. An EBIC image of the same region is given in Fig. 8 (b) and it demonstrates that the current collection efficiency varies between the bases and the tips of the pyramids as explained in our previous work [16]. Figure 9 (a) shows a high resolution LBIC map generated by the nano-LBIC system revealing similar features at around 500 nm scale. The observed difference between collected current at the bases and the tips can be explained by a number of effects: (i) there can be an enhanced light couple at the valleys than at the tips of the pyramids, thus generating more carriers, (ii) there is substantial laser damage to the pyramid tips when producing the selective emitter, (iii) lastly there are differences in the junction depth between the top and bottom of the pyramids, which would indicate larger travel length for carrier collection, as also noted in [16]. Such fine features shown here can hence prove the sub-micron mapping resolution.

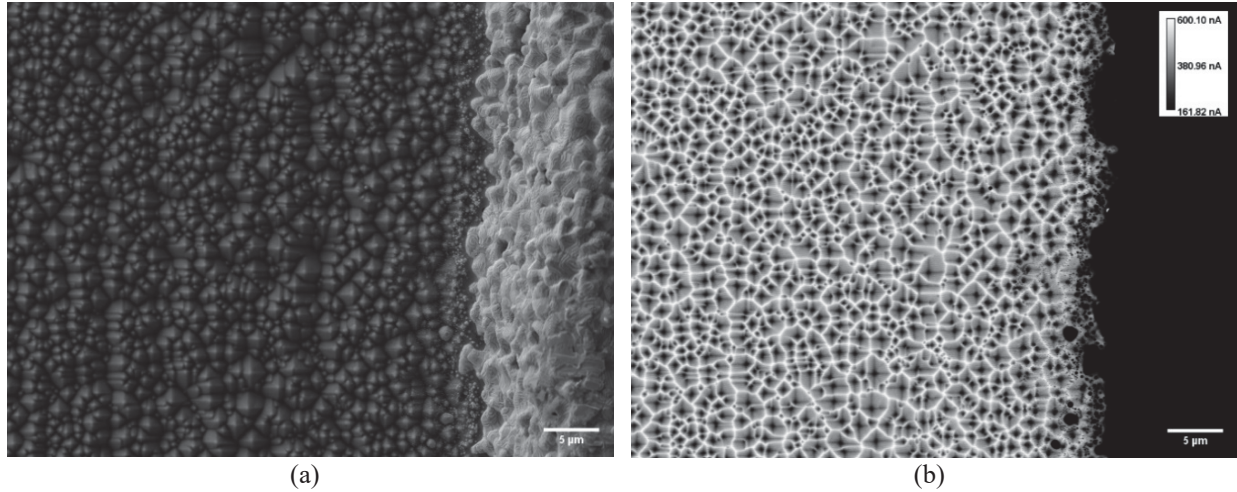


**FIGURE 8.** (a) SEM and (a) EBIC map of the region adjacent to the Ag finger, PERC cell A sample, EBIC beam energy 7.5 kV.

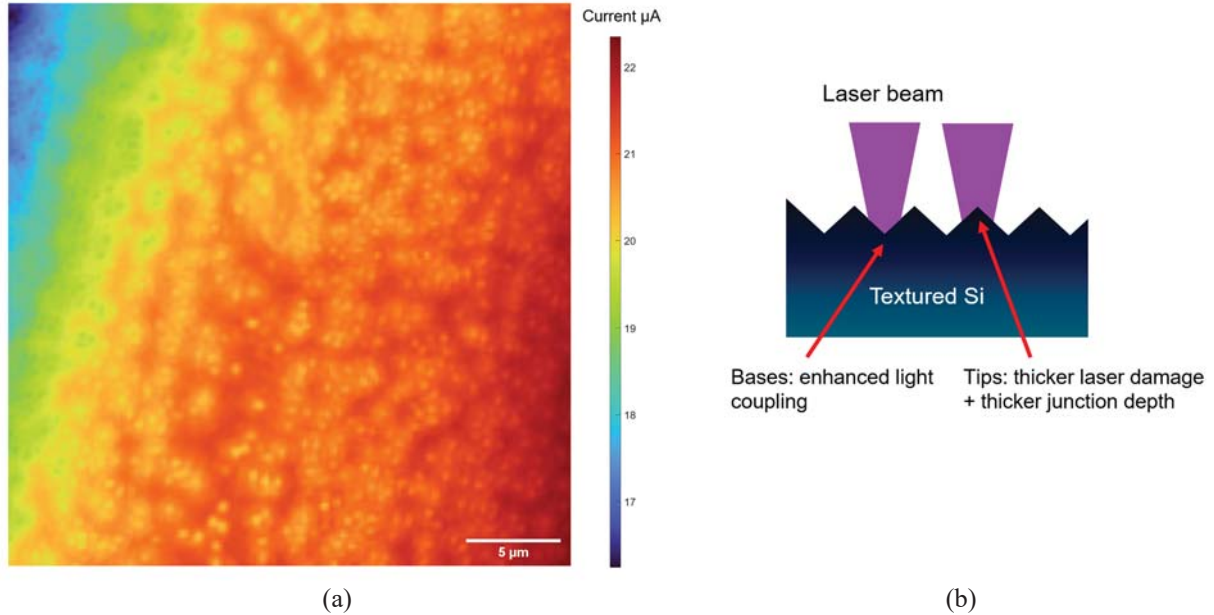


**FIGURE 9.** (a) 405 nm LBIC map of the laser doped selective emitter region adjacent to the Ag finger, pixel resolution 0.2  $\mu\text{m}$ , pixel dwell time 0.44s, PERC cell A sample. (b) Possible explanations for the higher current collected at the bases compared to tips.

## SUMMARY AND OUTLOOK

In this work we have used a commercial laser pick-up unit to build a nano-LBIC system with spatial resolution below one micrometre. Characterisation of industrial p-type mono PERC cells with laser doped selective emitters at different scales has been performed demonstrating the versatility of the system. By employing two different laser wavelengths we demonstrated the system capability in imaging and locating structural defects. These defects are well correlated to damage introduced during the laser doping process in the first hundreds of nanometres from the surface. A high spatial resolution LBIC map was constructed to reveal sub-micron features linked to the pyramidal surface texture. This demonstrated the nanoscale capability of this set up. All results were consistent with SEM micrographs and EBIC images as two relatively more complicated techniques used as benchmark to evaluate reliability and

accuracy of the system. Our future work will concentrate on exploiting the spatial resolution limit of the technique, calibration of laser sources for further interpretation of the current maps, and application of this system on other silicon cell structures.

## ACKNOWLEDGMENTS

Y. Shi and M Yu would like to thank the China Scholarship Council for funding their doctoral programs. R. S. Bonilla was supported by the Royal Academy of Engineering under the Research Fellowship scheme and acknowledges the support from the EPSRC Postdoctoral Fellowship EP/ M022196/1. This work was supported by the Black Silicon Photovoltaics project (Grant No. EP/R005303/1), Villum Experiment (Grant No. 00023116), the Danish National Research Foundation (DNRF122), and Villum Foundation (Grant No. 9301) for Intelligent Drug Delivery and Sensing Using Microcontainers and Nanomechanics (IDUN).

## REFERENCES

1. J. Marek, *J. Appl. Phys.* **55** (2), pp. 318–326, (1984).
2. C. Donolato, *J. Appl. Phys.* **54** (3), pp. 1314–1322, (1983).
3. S. Martinuzzi, and M. Stemmer, *Mater. Sci. Eng. B* **24** (1–3), pp. 152–158, (1994).
4. R. Jain, S. Behera, K. P. Sreejith, A. Kottantharayil, P. K. Basu, and A. K. Sharma, In *2018 4th IEEE International Conference on Emerging Electronics, ICEE 2018*; Institute of Electrical and Electronics Engineers Inc., (2018).
5. T. Luka, M. Turek, C. Kranert, S. Großer, and C. Hagendorf, *Energy Procedia* **124**, pp. 759–766, (2017).
6. K. Sporleder, V. Naumann, J. Bauer, S. Richter, A. Hähnel, S. Großer, M. Turek, and C. Hagendorf, *Sol. Energy Mater. Sol. Cells* **201**, 110062, (2019).
7. M. Rinio, A. Yodyungyong, S. Keipert-Colberg, D. Borchert, and A. Montesdeoca-Santana, *Phys. status solidi* **208** (4), pp. 760–768, (2011).
8. K. Nishioka, T. Yagi, Y. Uraoka, and T. Fuyuki, *Sol. Energy Mater. Sol. Cells* **91** (1), 1–5, (2007).
9. M. Breitwieser, F. D. Heinz, A. Büchler, M. Kasemann, J. Schön, W. Warta, and M. C. Schubert, *Sol. Energy Mater. Sol. Cells* **131**, pp. 124–128, (2014).
10. A. Büchler, H. Nagel, M. Breitwieser, S. Kluska, F. D. Heinz, M. C. Schubert, M. Glatthaar, and S. Glunz, In *2017 IEEE 44th Photovoltaic Specialist Conference (PVSC)*; (2017).
11. J. Martín, C. Fernández-Lorenzo, J. A. Poce-Fatou, and R. Alcántara, *Prog. Photovoltaics Res. Appl.* **12** (4), pp. 283–295, (2004).
12. F. J. Navas, R. Alcántara, C. Fernández-Lorenzo, and J. Martín-Calleja, *Rev. Sci. Instrum.* **81** (3), p. 035108-035108–035110.
13. Blu-ray Disc Association, White Paper Blu-ray Disc™ Format <http://www.blu-raydisc.com/Assets/Downloadablefile/BD-ROMwhitepaper20070308-15270.pdf>.
14. E. E. Te Hwu, and A. Boisen, *ACS Sensors*. American Chemical Society July 27, 2018, pp. 1222–1232.
15. F. S. Russell-Pavier, L. Picco, J. C. C. Day, N. R. Shatil, A. Yacoot, and O. D. Payton, *Meas. Sci. Technol.* **29** (10), 105902, (2018).
16. M. Yu, R. Zhou, P. Hamer, D. Chen, X. Zhang, P. P. Altermatt, P. R. Wilshaw, and R. S. Bonilla, *Sol. Energy* **211**, pp. 1214–1222, (2020).
17. J. Weber, S. Gutscher, S. Lohmüller, E. Lohmüller, and A. A. Brand, In *Proc. 35th Eur. Photovolt. Sol. Energy Conf. Exhib.*; (2018); pp. 379–384.
18. R. Zhou, M. Yu, D. Tweddle, P. Hamer, D. Chen, B. Hallam, A. Ciesla, P. P. Altermatt, P. R. Wilshaw, and R. S. Bonilla, *J. Appl. Phys.* **127** (2), 024502, (2020).
19. M. A. Green, *Sol. Energy Mater. Sol. Cells* **92** (11), pp. 1305–1310, (2008).